Evolution of the Distribution of Upper-Tropospheric Humidity over the Indian Ocean: Connection with Large-Scale Advection and Local Cloudiness

Thomas Garot, Hélène Brogniez, Renaud Fallourd, Nicolas Viltard

Evolution of the Distribution of Upper-Tropospheric Humidity over the Indian Ocean: Connection with Large-Scale Advection and Local Cloudiness

THOMAS GAROT, HÉLÈNE BROGNIEZ, RENAUD FALLOURD, AND NICOLAS VILTARD

LATMOS/IPSL, UVSQ Université Paris–Saclay, UPMC Université Paris 06, CNRS, Guyancourt, France

(Manuscript received 6 June 2016, in final form 24 February 2017)

ABSTRACT

The spatial and temporal distribution of upper-tropospheric humidity (UTH) observed by the Sounder for Atmospheric Profiling of Humidity in the Intertropics by Radiometry (SAPHIR)/*Megha-Tropiques* radiometer is analyzed over two subregions of the Indian Ocean during October–December over 2011–14. The properties of the distribution of UTH were studied with regard to the phase of the Madden–Julian oscillation (active or suppressed) and large-scale advection versus local production of moisture. To address these topics, first, a Lagrangian back-trajectory transport model was used to assess the role of the large-scale transport of air masses in the intraseasonal variability of UTH. Second, the temporal evolution of the distribution of UTH is analyzed using the computation of the higher moments of its probability distribution function (PDF) defined for each time step over the domain. The results highlight significant differences in the PDF of UTH depending on the phase of the MJO. The modeled trajectories ending in the considered domain originate from an area that strongly varies depending on the phases of the MJO: during the active phases, the air masses are spatially constrained within the tropical Indian Ocean domain, whereas a distinct upper-tropospheric (200–150 hPa) westerly flow guides the intraseasonal variability of UTH during the suppressed phases. Statistical relationships between the cloud fractions and the UTH PDF moments of are found to be very similar regardless of the convective activity. However, the occurrence of thin cirrus clouds is associated with a drying of the upper troposphere (enhanced during suppressed phases), whereas the occurrence of thick cirrus anvil clouds appears to be significantly related to a moistening of the upper troposphere.

1. Introduction

Water vapor is the primary greenhouse gas in the troposphere and plays an important role in the atmospheric energy budget. Understanding and characterizing the physical processes that regulate the distribution of water vapor is an important step to further improve our knowledge of the climate system and thus to reduce the uncertainties associated with fast climate variations (IPCC 2013). Estimates of climate sensitivity depend critically on the radiative feedbacks associated with water vapor. As expressed by the Clausius–Clapeyron law, a warmer atmosphere can contain more water vapor. An external forcing that warms the surface thus leads to an increase in water vapor, resulting in an amplifying feedback mechanism (Allan et al. 2003; Colman 2003; Soden and Held 2006; Dessler and Sherwood 2009). As stated by Sherwood et al. (2006) and Ryoo et al. (2008), the distribution of the tropical free tropospheric relative humidity is the result of a slow uniform subsidence that overall dries the troposphere and of random–local and rapid moistening events associated with deep convection.

Numerous studies have highlighted a strong relationship between the upper-tropospheric humidity (UTH) distribution and the large-scale dynamics on monthly (Picon and Desbois 1990; Schmetz et al. 1995) and daily time scales (Pierrehumbert and Roca 1998; Brogniez and Pierrehumbert 2006; Dessler and Minschwaner 2007). Several studies have also focused on the relationship between the UTH and cloud cover. Gray et al. (1975), Soden and Fu (1995), Udelhofen and Hartmann (1995), and Roca et al. (2002) have highlighted a positive relationship between the occurrence of tropical convective clouds and UTH. Sassi et al. (2001) underlined the strong spatial coherence between UTH and a cold cloud cover (defined by the 11-μm brightness temperature below 230 K for monthly and daily means), which supports the ventilation of the upper troposphere by tropical convection and highlights the role of the Hadley and Walker circulations in the vertical transport of moisture. Zelinka and Hartmann (2009) have shown that the deep convective

Corresponding author: Thomas Garot, thomas.garot@latmos.ipsl.fr

DOI: 10.1175/JAMC-D-16-0193.1

clouds in the tropics produce cirrus anvils together with an increase in UTH. Results obtained from flight observations by Perry and Hobbs (1996) over the midlatitudes and by Laird (2005) in the tropics suggest that small-to-medium-sized isolated cumulus clouds change the distribution of humidity in the surrounding clear areas because of the detrainment from gravity waves. Furthermore, tropical cirrus anvils are associated with a moister upper troposphere according to 6-hourly satellite observations (Soden 2004; Luo and Rossow 2004). Over areas where the sea surface temperature is warmer than 300 K, strong positive correlations between the annual means of UTH and the ice water content of tropical cirrus have been observed (Su et al. 2006). Chung et al. (2007) have shown that over tropical Africa and the adjacent tropical Atlantic Ocean, the diurnal variations of UTH are shifted by a few hours from those of deep convection and cirrus anvil clouds. Their study suggests that the evolution of cirrus anvil clouds and UTH is mainly related to the growing and decaying of deep convective clouds.

Most of these studies explore the influences of various parameters such as cloudiness or winds on the variability of the UTH using spatial mean values varying from annual to 6-hourly time scales. The role of large-scale processes and cloud-related processes on the distribution of UTH is analyzed here, taking advantage of the sampling offered by the *Megha-Tropiques* satellite, which is increased relative to other polar-orbiting platforms. The analysis is carried out over the Indian Ocean, where an intense convective activity during winter is associated with the Madden–Julian oscillation (MJO; Madden and Julian 1971, 1972). The MJO is the dominant mode of intraseasonal variability in the tropical atmosphere, with its main features propagating eastward over the Indian and Pacific Oceans [see Zhang (2013) for a comprehensive review]. The origin and the triggering of the MJO are open questions that has led to the deployment of several dedicated international field campaigns aiming at gathering observations of the ocean–atmosphere parameters, such as the Tropical Ocean and Global Atmosphere Coupled Ocean–Atmosphere Response Experiment (TOGA COARE; during the winter 1992/93) and the Cooperative Indian Ocean Experiment on Intraseasonal Variability in the Year 2011/Dynamics of the Madden–Julian Oscillation/Atmospheric Radiation Measurement Program Madden–Julian Oscillation Investigation Experiment (CINDY/DYNAMO/AMIE; during the winter 2011/12 and detailed below). The purpose of the present study is to understand how convective activity and the MJO impact the UTH rather than to understand the properties of the MJO and its triggering.

The launch of the *Megha-Tropiques* satellite in October 2011 was synchronized with the beginning of a new season of MJO events. With an inclined orbit at the equator (20°), this satellite offers a unique sampling of the entire tropical belt (30°N–30°S) with three to five overpasses on average per day for a specific location (Desbois et al. 2007). *Megha-Tropiques* is an Indo-French mission designed to document the energy and water cycles of the tropical belt. The satellite carries two microwave sensors, Multi-Frequency Microwave Scanning Radiometer (MADRAS) and Sounder for Atmospheric Profiling of Humidity in the Intertropics by Radiometry (SAPHIR), and a broadband visible and infrared Scanner for Radiation Budget (ScaRaB). The instrument of interest here is SAPHIR, a cross-track scanning sounder operating in the 183.3-GHz water vapor absorption line and dedicated to tropospheric humidity profiling. A review of the *Megha-Tropiques* mission with a description of the instruments and their performances is given in Roca et al. (2015). Roca et al. (2015) also present the impact of the original precession cycle of the satellite on the day-to-day sampling, which differs according to the latitude band; in addition to a regular backward shift of the local time of observations, the sampling is performed in packets composed of three to five consecutive overpasses that are 102 min (at 12°N–S) to roughly 20 h (at 25°N–S) away from each other.

The data used in this study are presented in section 2 and consist of the SAPHIR UTH, the radiosounding measurements collected during the CINDY/DYNAMO/AMIE campaign, the thermodynamic fields from the European Centre for Medium-Range Weather Forecasts (ECMWF) interim reanalysis (ERA-Interim) used to perform back-trajectory computations, and the cloud classification product used to define the cloudiness. Section 3 is dedicated to the description of the MJO and its intraseasonal variability according to the statistical moments of the distribution of UTH. The relationship between satellite measurements of UTH and large-scale dynamics and cloudiness according to the convective activity is analyzed in section 4. The results are discussed in section 5, and future studies are suggested.

2. Data

The variability of the UTH is analyzed using four datasets: the SAPHIR observations of UTH, the relative humidity (RH) measured by upper-air soundings, the dynamic and thermodynamic fields produced by the ERA-Interim model, and the cloud classifications defined from a series of geostationary imagers.

a. Upper-tropospheric humidity from SAPHIR

SAPHIR is a cross-track scanning sounder that measures the upwelling microwave radiation in six channels spanning the 183.31-GHz water vapor absorption line,

from the upper troposphere (183 ± 0.2 GHz; channel 1) down to above the boundary layer (183 ± 11 GHz; channel 6), allowing for a vertical sounding of the atmosphere (Brogniez et al. 2013). As for the Advanced Microwave Sounding Unit B (AMSU-B) and Microwave Humidity Sounder (MHS), SAPHIR measurements can be used to estimate the UTH (in percent, defined with respect to liquid water). Indeed, microwave brightness temperatures (BTs) measured close to the center of the 183.31-GHz line are sensitive to the layer-averaged relative humidity of the upper troposphere, similar to the 6.3-μm channels (Soden and Bretherton 1993). The relationship between BT and UTH can be written as

$$\ln(\mathrm{UTH}) = a \times \mathrm{BT} + b, \tag{1}$$

where BT is in kelvins, and the slope and intercept (a and b) of the equation are defined once on the basis of a learning phase [see Brogniez et al. (2015) for details]. In fact, the configuration of SAPHIR allows for the definition of three UTHs ($\mathrm{UTH}i_{\mathrm{SAPHIR}}$, $i = 1, \ldots, 3$) that slightly overlap and overall cover the region 100–700 hPa [see Fig. 1 of Brogniez et al. (2015)]. $\mathrm{UTH1_{SAPHIR}}$ is obtained from the BT of channel 1, at 183 ± 0.2 GHz, and covers roughly the layer 100–500 hPa. $\mathrm{UTH2_{SAPHIR}}$ is obtained from the BT of channel 2, at 183 ± 1.1 GHz, and covers roughly the layer 200–600 hPa. $\mathrm{UTH3_{SAPHIR}}$ is obtained from the BT of channel 3, at 183 ± 2.8 GHz, and goes down to 750 hPa. The vertical pressure range covered by the UTHs depends on the moisture content of the atmospheric columns: the drier the atmosphere is, the thicker is the atmospheric layer from which the radiation originates. Therefore, the spaceborne observations of UTH are not associated to a fixed range of pressure but to the upper troposphere (100–400 hPa) in the moistest cases and extend to the free troposphere (100–800 hPa) in the driest conditions. Brogniez et al. (2015) compared these $\mathrm{UTH_{SAPHIR}}$ with reference UTHs computed from RH profiles ($\mathrm{UTH_{RS}}$) measured by radiosoundings from two field campaigns: the CINDY/DYNAMO/AMIE field experiment (see description in section 2b) and the *Megha-Tropiques* validation campaign. The latter resulted in the collection of 54 radiosoundings collocated in space and time with SAPHIR measurements around Ouagadougou, Burkina Faso, during the summer of 2012. This comparison between the $\mathrm{UTH_{SAPHIR}}$ and the $\mathrm{UTH_{RS}}$ showed a very good consistency between the two estimates of UTHs, with global differences lower than 2% on average and root-mean-square errors of the linear regressions ranging between 0.92% (for $\mathrm{UTH1_{SAPHIR}}$) and 4.71% (for $\mathrm{UTH3_{SAPHIR}}$).

b. *Reference measurements from radiosoundings*

The CINDY/DYNAMO/AMIE international field experiment was conducted over the Indian Ocean during the period October 2011–March 2012 to address the mechanisms responsible for the MJO. During this experiment, intensive soundings of the atmosphere were performed using radar, radiosondes, and microphysics probes. These soundings were combined with data from a mooring network that collected in situ observations of the atmosphere and ocean. The key scientific questions of CINDY/DYNAMO/AMIE are 1) the evolution of moisture in the troposphere, more specifically during the initiation stage of the MJO; 2) the relationships between evolution of the MJO and mesoscale convective systems; and 3) the roles of equatorial waves and sea surface conditions in the development and evolution of the MJO (Johnson and Ciesielski 2013). Figure 1 shows the sounding network that includes two quadrilateral arrays in which more intense measurements were performed (from four to eight soundings per day). In the following, these two arrays are the northern sounding array (NSA) and southern sounding array (SSA). They are located around (72°–80°E, 0°–8°N) and (72°–80°E, 0°–8°S), respectively. The instruments in these sounding arrays were fully operational for most of the 1 October–15 December 2011 period, as documented by Johnson and Ciesielski (2013). These two arrays were limited spatially by the two research vessels (R/Vs; *Mirai* and *Revelle*) that had to perform port calls after this period. An objective analysis of the upper-air soundings of NSA and SSA was performed by the Colorado State University (CSU) Mesoscale Dynamics Group to produce a regular dataset of RH (1°, 25 hPa, 3 h) using multiquadratic interpolation and later averaged spatially over the two NSA and SSA domains (Johnson and Ciesielski 2013). To compare these reference measurements with the $\mathrm{UTH_{SAPHIR}}$, temperature and specific humidity profiles from the radiosoundings were converted into UTH ($\mathrm{UTH_{CDA}}$) following the model-to-satellite approach (Morcrette 1991) as in Brogniez et al. (2015). From the thermodynamic profiles, synthetic SAPHIR BTs were computed with Radiative Transfer for Television and Infrared Observation Satellite Operational Vertical Sounder (RTTOV)-11 radiative code (Eyre 1991; Matricardi et al. 2004; Saunders et al. 2013). The simulated BT was then interpreted in terms of UTH using Eq. (1).

c. *ERA-Interim*

ERA-Interim is a dynamical reanalysis of meteorological observations constructed by the ECMWF using

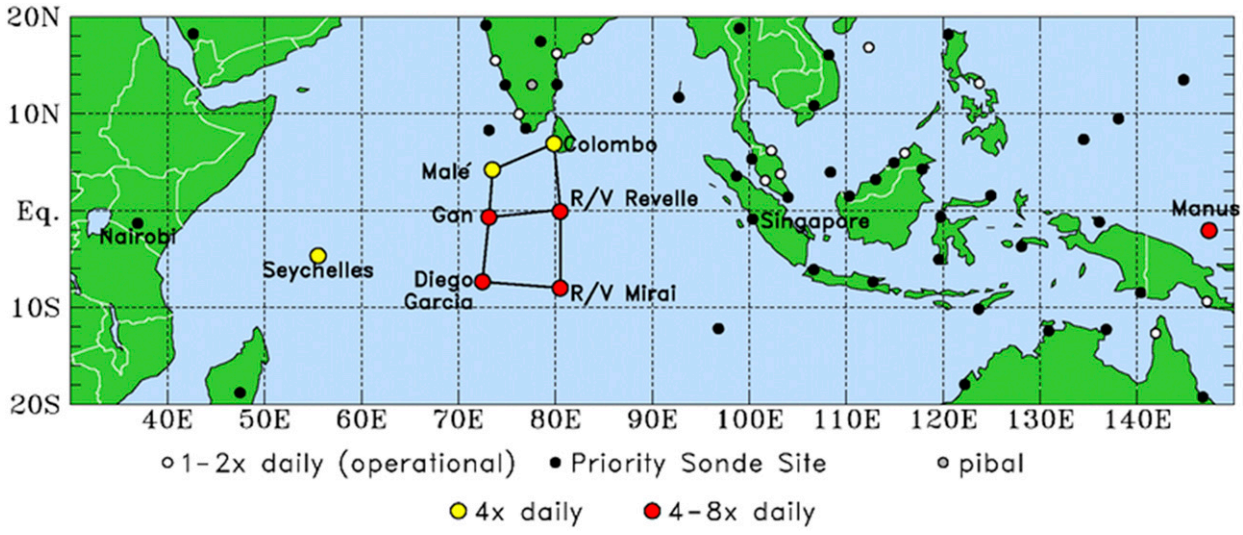

FIG. 1. The CINDY/DYNAMO/AMIE sounding network for the period OND 2011 [from Johnson and Ciesielski (2013)]. The two experimental sounding arrays NSA and SSA are each outlined. The yellow and red dots are the main sounding sites with four and eight launches per day, respectively.

satellite observations and supplemented by in situ measurements from aircrafts, ocean buoys, and surface platforms (Dee et al. 2011). A large majority of the sounding observations performed during CINDY/DYNAMO/AMIE [October–December (OND) 2011] were transmitted to the ECMWF operational center (Johnson and Ciesielski 2013). ERA-Interim fields are available at 60 vertical levels extending from the surface up to 0.1 hPa, every 6 h (0000, 0600, 1200, and 1800 UTC). In the present study, the 0.75° gridded fields of temperature and specific humidity were used. UTHs were also computed from the ERA-Interim profiles (UTH_{ERA}) with the model-to-satellite method described in the previous paragraph. In the present work, UTH_{ERA} were used to qualitatively evaluate the temporal variability of UTH_{SAPHIR} in terms of phase and amplitude of variation in 2011 when ECMWF assimilated the radiosoundings of the various observing periods of CINDY/DYNAMO/AMIE and in 2012–14 when only the regular soundings of the area were assimilated. It is noteworthy that at the time of this study, the assimilation of the SAPHIR observations by the ECMWF assimilation system was ongoing (A. Geer, ECMWF, 2015, personal communication). Relative to ERA-40 (the previous version of the reanalysis), ERA-Interim features substantial improvements in the representation of the hydrological cycle, the quality of the stratospheric circulation, and the consistency in time of the reanalyzed fields (Dee and Uppala 2009). However, ERA-Interim has a cold bias in the upper troposphere introduced by Microwave Sounding Unit (MSU) instrument errors, which could lead to an overestimation of UTH (Dee and Uppala 2009).

d. Cloud classification

The temporal variability of the occurrence of each type of cloud is described using the cloud type product developed within the Satellite Application Facility on Support to Nowcasting (SAFNWC; Derrien and Le Gléau 2003) to support weather forecasting activities. This software relies on multispectral (visible and infrared channels) threshold tests applied at the pixel level and adapted to the spectral functions of four geostationary satellites: Meteorological Satellite (Meteosat) Second Generation (MSG), Geostationary Operational Environmental Satellite (GOES)-East and GOES-West, and Multifunctional Transport Satellites (MTSATs). The algorithm also uses the pressure thresholds from the International Satellite Cloud Climatology Project (ISCCP; Rossow and Schiffer 1991). This provides a cloud classification with 10 classes detailed in Table 1. The current algorithm does not separate stratiform and cumuliform clouds because of the unavailability of a phase flag, instead classifying all clouds as opaque and cumuliform (Derrien and Le Gléau 2010). The evaluation of this classification using collocated Cloud–Aerosol Lidar with Orthogonal Polarization (CALIOP) observations [on *Cloud–Aerosol Lidar and Infrared Pathfinder Satellite Observations* (*CALIPSO*), part of the afternoon constellation of Earth Observing System (EOS) satellites (A-Train)] by Sèze et al. (2015) has shown a 20% nondetection of low-level clouds due to broken cloud coverage, and an overall 10% nondetection of some multilayered cloudiness (at least two cloud layers separated by more than 100 hPa, such as cirrus

TABLE 1. Cloud classes from the SAFNWC classification (Derrien and Le Gléau 2010) and the six cloud classes used in this study.

SAFNWC classification	Choice of classes
Cloud-free land no contamination by snow/ice-covered surface	Clear sky
Cloud-free sea no contamination by snow/ice-covered surface	
Land contaminated by snow	
Sea contaminated by ice/snow	
Very low and cumuliform/stratiform clouds ($P_{top} > 800$ hPa)	Low clouds
Low and cumuliform/stratiform clouds (800 hPa $> P_{top} >$ 650 hPa)	
Medium and cumuliform/stratiform clouds (650 hPa $> P_{top} >$ 450 hPa)	Medium clouds
High opaque and cumuliform/stratiform clouds (450 hPa $> P_{top} >$ 300 hPa)	High clouds
Very high opaque and cumuliform/stratiform clouds ($P_{top} <$ 300 hPa)	
High semitransparent thin clouds	Cirrus
High semitransparent meanly thick clouds	
High semitransparent thick clouds	
High semitransparent above low or medium clouds	
Fractional clouds (subpixel water clouds)	Fractional clouds

above low- or midlevel clouds). Here, the 10 cloud classes have been aggregated into 6 main classes according to the cloud-top pressure P_{top}: 1) clear sky, 2) low clouds ($P_{top} > 650$ hPa), 3) medium clouds ($650 > P_{top} > 450$ hPa), 4) high clouds ($P_{top} < 450$ hPa), 5) high semitransparent clouds (cirrus), and 6) fractional clouds. These classes are projected within SAPHIR pixels with a space–time nearest-neighbor approach, restricted in time to 25 min (there are 20 geostationary pixels on average in an $\sim 10 \times 10$ km^2 SAPHIR pixel at nadir), thus allowing for the study of the relationship between the occurrence of cloud types and the UTH distribution.

3. UTH variability over the Indian Ocean during the winters 2011–14

a. General description of the convective activity during Madden–Julian oscillations

The MJO is the main driver of the fluctuations of tropical weather on weekly to monthly time scales over the Indian Ocean and during boreal winter. The MJO can be characterized as an eastward moving ''pulse'' of clouds and rainfall near the equator that typically occurs every 30 to 60 days. It influences the global atmosphere, including the monsoon onset, the tropical cyclogenesis, and the occurrence of severe rainfall events (Wheeler et al. 2009; Camargo et al. 2009; Pai et al. 2011; Zhang 2013). Figure 2 shows the average geographical positions of convective clouds between October and December over the period 1974–2009 using the multivariate MJO index of Wheeler and Hendon (2004). This index decomposes the MJO into eight phases according to the location of enhanced convective signals analyzed from the outgoing longwave radiation (OLR) and low-level zonal winds. This figure is taken from the Australian Bureau of Meteorology (BoM; http://www.bom.gov.au/climate/mjo/) and represents the interpolated OLR data from the National Oceanic and Atmospheric Administration (NOAA) as well as the 850-hPa horizontal wind field (temporal anomaly with respect to the seasonal average; Wheeler et al. 2009). This figure helps to identify the convective clouds responsible for a strong reduction of the thermal emission of radiation to space. Therefore, during phases 1–4, the convective activity is mainly located over the Indian Ocean, at the tip of the Indian continent, as shown in Fig. 2. During phases 5–8, the convective activity is located over the western Pacific, and there is clearly less enhanced convection over the Indian Ocean. Such an index is provided on a near-real-time basis by the BoM and is used as a proxy to analyze the active (phases 1–4) and suppressed (phases 5–8) convective periods of the MJO over the NSA and SSA domains.

b. Temporal signature of the MJO convective activity in UTH

Johnson and Ciesielski (2013) have shown that the three convective phases of the MJO observed during the CINDY/DYNAMO/AMIE campaign are clearly visible in the NSA and SSA, with a strong modulation observed in the patterns of precipitation over the former, while briefer episodes of precipitation occurred over the latter. These episodes were most probably related to the convective activity of the intertropical convergence zone. The development phases of the MJO events of October and November 2011 were both characterized by a 2-week period of gradual moistening of the low to midtroposphere. During these onset phases, low-level flows were of opposite directions, with westerly and easterly flows, respectively, observed prior to the October and November events. Finally, the observed patterns of RH, low-level wind field divergence, and vertical motions in the two sounding arrays seem to support the assumption of an evolution of the cloud types from shallow cumulus into congestus and deep convective clouds. Because of this strong MJO signal in the CINDY/DYNAMO/AMIE radiosoundings, UTH_{CDA} and UTH_{SAPHIR} have been compared over OND 2011 to check whether the UTH_{SAPHIR} is suitable for the study of contrasted convective activities. Figure 3 illustrates this comparison using a Taylor diagram, which is a polar representation based on the Bravais–Pearson correlation coefficient (R, proportional to the

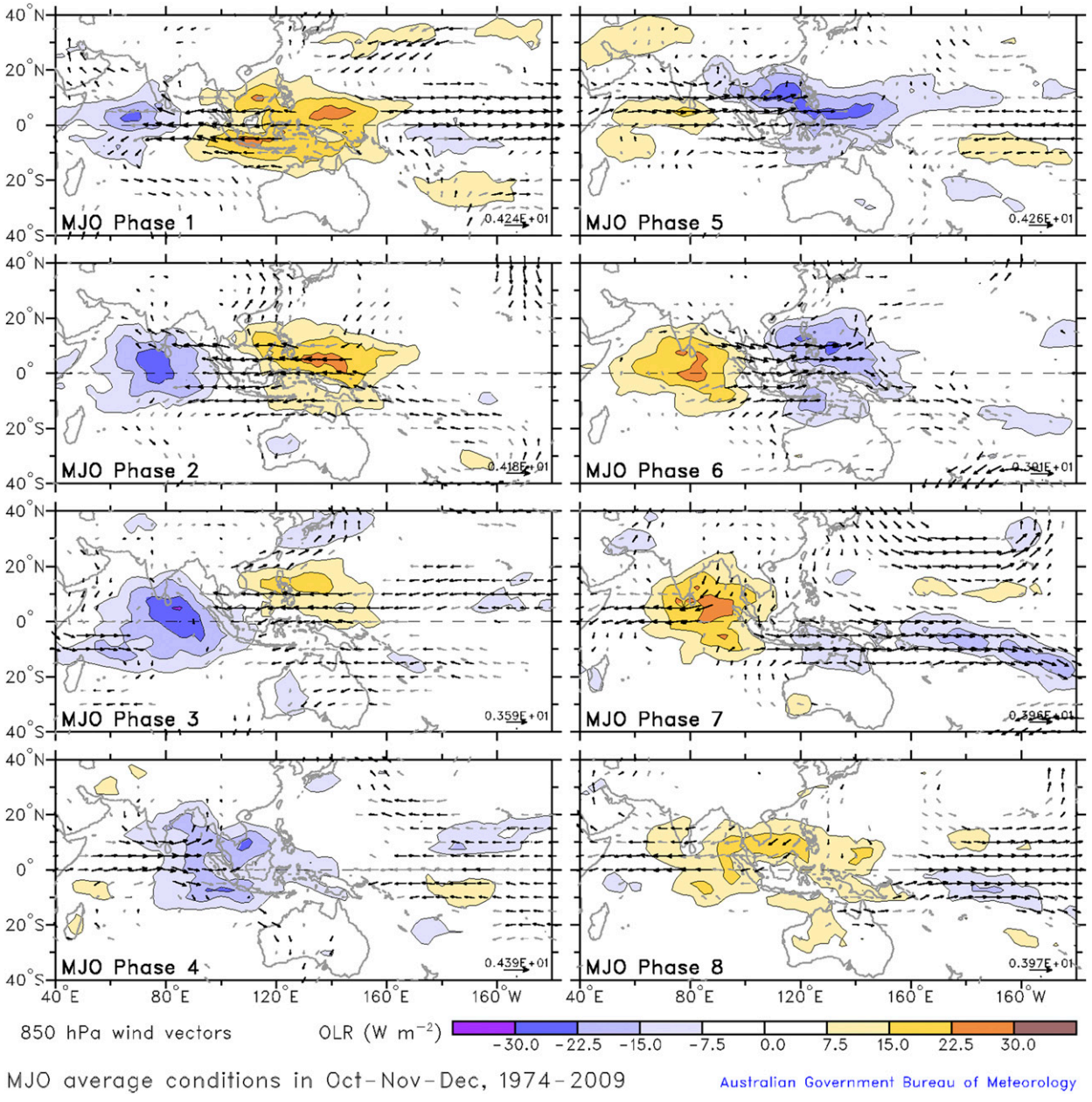

FIG. 2. Average conditions of OLR (W m^{-2}; from the interpolated OLR NOAA dataset) and of the 850-hPa wind field vectors (m s^{-1}) with respect to the expected cloudiness associated to MJO. The blue areas indicate higher convective activity than normal, whereas the yellow areas indicate lower convective conditions than normal. The direction and length of the arrows indicate the direction and strength of the seasonal wind anomaly with a reference magnitude arrow in the bottom right of each panel. The figure is extracted from the Australian BoM.

polar angle defined with respect to the abscissa) and on the normalized standard deviation (NSD; proportional to the distance from the center of the diagram). A Taylor diagram highlights simultaneous variability and bias issues (Taylor 2001). The quantities R and NSD are defined as follows:

$$R = \frac{\frac{1}{n}\sum_{i=1}^{n}[\mathrm{UTH}_{\mathrm{CDA}}(i) - E(\mathrm{UTH}_{\mathrm{CDA}})][\mathrm{UTH}_{\mathrm{SAPHIR}}(i) - E(\mathrm{UTH}_{\mathrm{SAPHIR}})]}{\sigma(\mathrm{UTH}_{\mathrm{CDA}})\sigma(\mathrm{UTH}_{\mathrm{SAPHIR}})}, \quad (2)$$

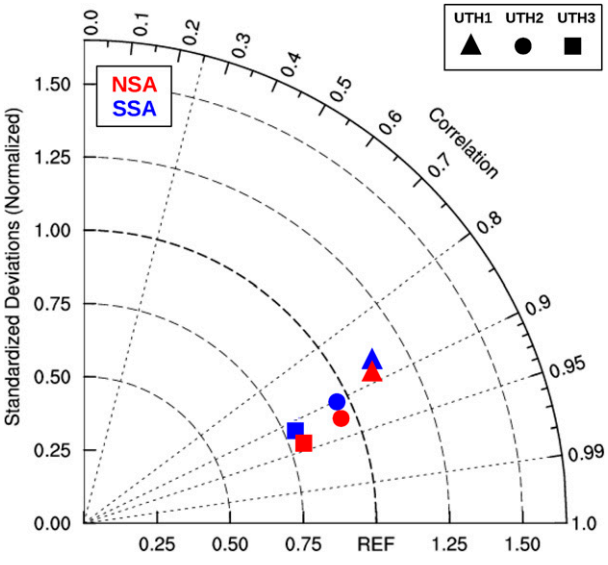

FIG. 3. Taylor diagram describing the similarities between the UTHs from SAPHIR and the UTH_{CDA} over NSA (red), SSA (blue), and during OND 2011. UTH_{CDA} is considered as the reference (indicated by REF). Correlations are significant at 0.25 according to a 1% risk t test.

$$\mathrm{NSD} = \sqrt{\frac{1}{n}\sum_{i=1}^{n}[\mathrm{UTH}_{\mathrm{CDA}}(i) - \mathrm{UTH}_{\mathrm{SAPHIR}}(i)]^2}, \qquad (3)$$

where n is the number of individuals, σ is the standard deviation, and E is the average value.

Here, for each *Megha-Tropiques* overpass over NSA and SSA, the data closest in time to UTH_{CDA} are selected within a time window of 1.5 h (two soundings are separated by 3 h). Figure 3 shows a strong similarity between UTH_{SAPHIR} and UTH_{CDA} for the three atmospheric layers with values of R overall greater than 0.85. While $UTH3_{CDA}$ has too little intraseasonal variability relative to $UTH3_{SAPHIR}$ (NSD = 0.8), $UTH1_{CDA}$ features larger variations than those observed in $UTH1_{SAPHIR}$ (NSD = 1.1), and the amplitude of $UTH2_{CDA}$ variations is the closest to the amplitude of the observed $UTH2_{SAPHIR}$ variations (NSD = 0.9). Despite some differences of amplitude, the high correlations between the $UTH1_{CDA}$ and $UTH1_{SAPHIR}$ demonstrates the possible use of the latter to perform MJO-related studies. This motivates the exploration of the observational capabilities of SAPHIR to analyze the patterns of variability of UTH according to MJO phases over OND periods during 2011–14.

Longitude–time Hovmöller diagrams of $UTH3_{SAPHIR}$ are shown in Fig. 4 for OND of 2011, 2012, 2013, and 2014 (results for the two other UTHs are identical; not shown). The data of UTH_{SAPHIR} are remapped into a regular 1° × 1° grid, and daily means are computed in order to highlight the intraseasonal variability and to smooth out the instantaneous observations. The meridional average is performed between 8°S and 8°N, the southernmost and northernmost limits of the NSA and SSA domains, respectively. For the four years, several eastward-propagating patterns of humidity can be observed. They are more marked in 2011 and 2014 than in 2012 and 2013. Considering the eastward structures and the frequency of oscillations (30 days), these patterns are clear signatures of MJO events.

Johnson and Ciesielski (2013) have shown that the MJO event of October 2011 and the one of November

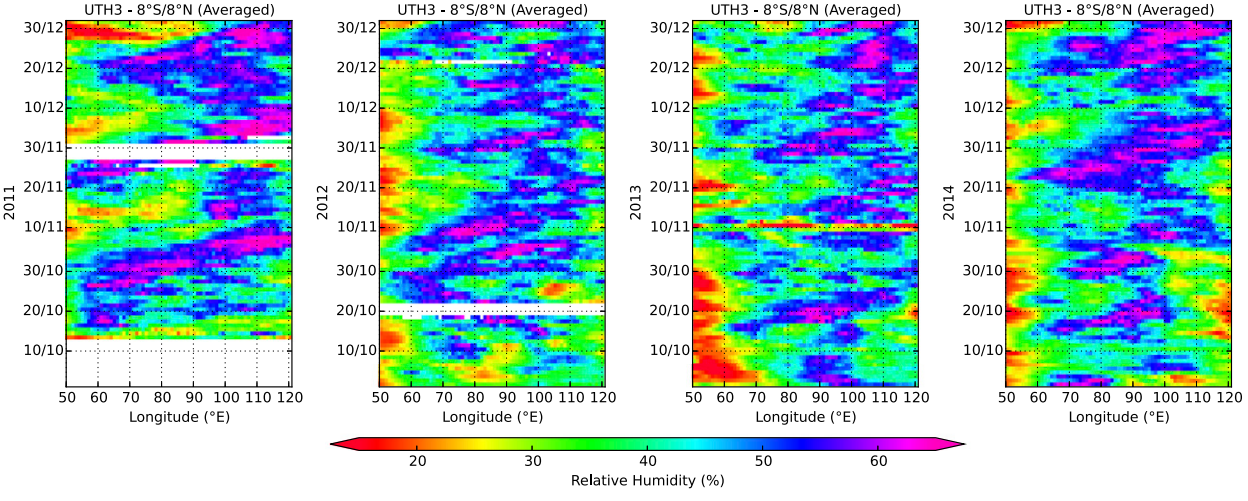

FIG. 4. Longitude–time Hovmöller diagrams of UTH3 from SAPHIR (remapped into 1° × 1 day) covering October–December from (far left) 2011 to (far right) 2014. Time increases upward. Latitudes are averaged over the NSA–SSA limits (8°N–8°S).

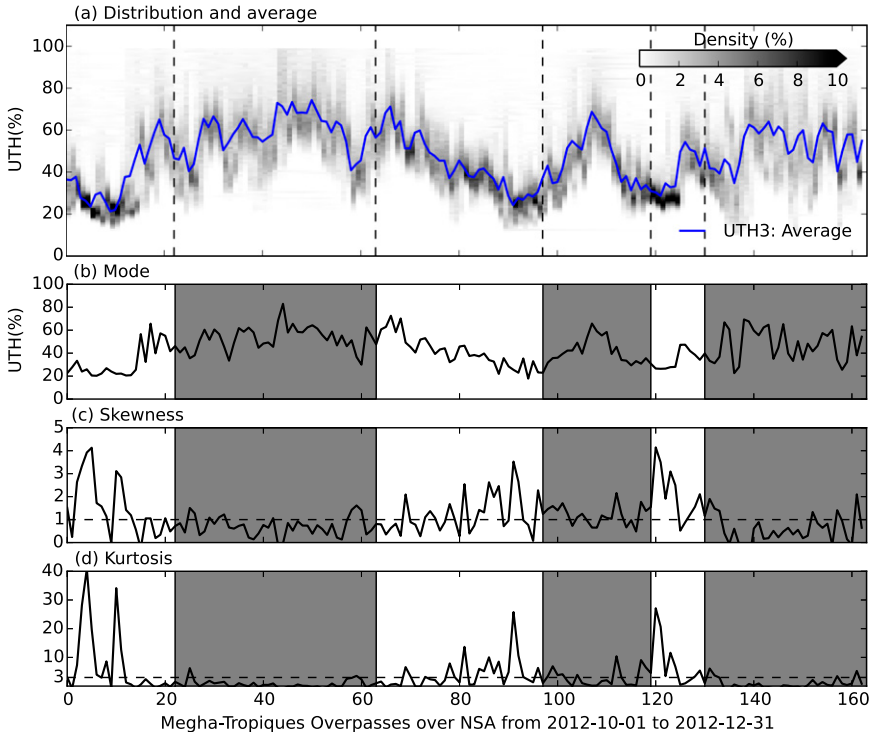

FIG. 5. The 1 Oct–31 Dec 2012 time series of (a) the general distribution of UTH3, using a density diagram; (b) mode; (c) skewness; and (d) kurtosis. The parameters are defined for each *Megha-Tropiques* overpass over the NSA region. The gray shaded areas are the periods of active MJO events identified by the Australian BoM. The horizontal dashed lines for skewness and kurtosis are a reference for a symmetric distribution.

2011 are rather different in terms of dynamics. A low-level westerly flow preceded the October event, while low-level easterlies preceded the November event, as stated previously. Here, the variability of UTH is only characterized in terms of convective activity, that is, in terms of active and suppressed phases, rather than in terms of dynamical regimes.

c. *Intraseasonal and interannual variability of UTH*

The temporal variability of the UTHs is further analyzed through the four moments of its spatial distribution within NSA and SSA: the average, the mode, the skewness (*S*; reflecting the asymmetry and the length of the tails of the distribution), and the kurtosis (*K*; measuring the peakedness). The definitions are provided in the appendix. As an example, Fig. 5 presents the time series of these four moments of $UTH3_{SAPHIR}$ (i.e., the relative humidity of the 300–750-hPa atmospheric layer) over the NSA area for the overpasses of *Megha-Tropiques* recorded during OND 2012. Note that the *x* axis represents the succession of the overpasses over the region rather than regular time series in order to enhance the relevant features. Indeed, the time interval between two points is sometimes 102 min and sometimes 20 h or more. The figure should therefore be used to identify bulk features over the three months. Gray shaded areas highlight the active phases of MJO identified over this period. The analysis of the four moments shows that the distribution of $UTH3_{SAPHIR}$ has different features depending on the convective activity. During the convectively active phases, the average and mode of $UTH3_{SAPHIR}$ reached values around 60% (close to ice saturation), and its distribution is mainly negatively skewed (Fig. 5c) and platykurtic (Fig. 5d). During the suppressed phases, the average and mode of $UTH3_{SAPHIR}$ have smaller values, reaching 20%–30% of RH, and its follows a law of distribution is overall positively skewed (Fig. 5c) and leptokurtic (Fig. 5d). These differences are summarized in Fig. 6, which features the distributions of UTH computed over both NSA and SSA, for all four OND periods (2011 through 2014) using PDFs. The distributions of UTHs computed over the active and the suppressed periods are distinguishable. During active (respectively suppressed) phases, the PDFs of the three layers of UTH_{SAPHIR} are negatively (positively) skewed. During the suppressed phases, the peak of the PDF of UTH1 is narrow, bell shaped, and located at RH ~ 25%. The skewness

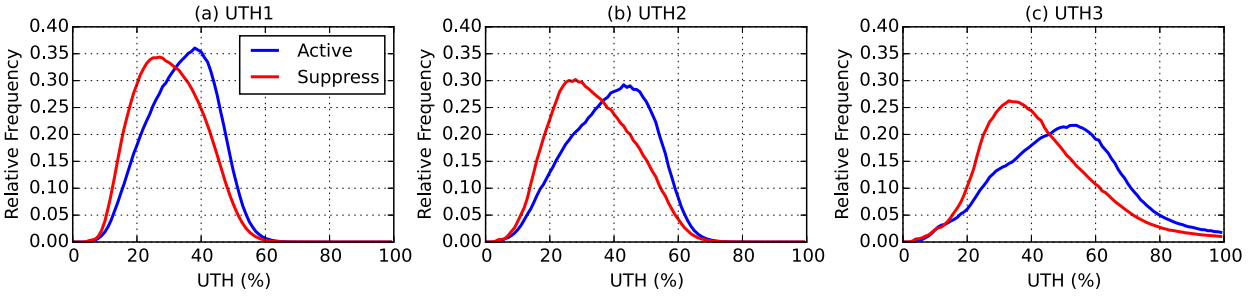

FIG. 6. PDFs for the three levels of UTH_{SAPHIR} over NSA and SSA during OND 2011, 2012, 2013, and 2014 depending on active (blue) or suppressed (red) phases of MJO.

increases smoothly toward the middle of the troposphere, the PDF of UTH3 peaking at RH ~ 35% with significant occurrences of higher values. For the active phases of enhanced convection, the peak of the PDF of UTH1 occurs at a higher value of RH (~40%), and its PDF is narrow, negatively skewed, and it increases to reach ~50% for UTH3; in this case, with lower RH values. These results are consistent with the overall description of bimodality of the tropical precipitable water by Zhang et al. (2003) as measured by a variety of observing systems. While Zhang et al. (2003) consider the tropics as a whole, here, we decompose the PDFs into one associated to an enhanced convective activity and another one without pronounced deep convection. Our results are also similar to the description of the tropical and subtropical RH based on the remapped RH field (250 hPa, 1° × 1°) estimated from Atmospheric Infrared Sounder (AIRS) measurements (climatological means and daily values) by Ryoo et al. (2008). Focusing on the eastern Indian Ocean and the western Pacific, they especially underlined the role of the modulation by the MJO of advection from subtropical anticyclones, located slightly west of the convective clouds.

4. Role of large-scale advection and local cloudiness

a. *Assessment of the advection of air masses*

Since the convective activity is one of the main drivers of the UTH distribution, the suppressed and active phases of the MJO are hereafter considered separately within the two sounding arrays NSA and SSA. The advection of air is analyzed using a back-trajectory Lagrangian transport model, which provides the origin of the air parcels finally reaching either the NSA or the SSA. This model is a "last-saturation" type where water vapor is considered as a passive and nondiffusive tracer (Pierrehumbert and Yang 1993). In the absence of sources or sinks of humidity, the amount of water vapor can be considered as conserved along the trajectory. The entire moisture source is in the saturated boundary layer (pressure > 800 hPa), and the deep convection transports this saturated air upward to make it available for the large-scale flows. This paradigm defines the coordinates where the last saturation occurs: it is the location within the trajectory that has the coldest air temperature that translates into the minimum water vapor mixing ratio, according to the Clausius–Clapeyron law. This defines the location of final dehydration of the air mass along its transport. The model successfully reproduces the observed distribution of tropospheric humidity based on analyses or reanalyses (Pierrehumbert and Roca 1998; Galewsky et al. 2005; Dessler and Minschwaner 2007; Brogniez et al. 2009). The advection–condensation paradigm is also used to study the stratospheric water vapor (e.g., Liu et al. 2010). Such a model contains no microphysics. It also neglects the redistribution of excess moisture that condenses as the air parcel penetrates a subsaturated environment (the precipitation efficiency is assumed to be 100%) as well as the mixing among air parcels induced by small-scale turbulences that are smaller than the actual horizontal and vertical resolution of the model, as highlighted by Pierrehumbert et al. (2007) and Sherwood et al. (2010). The dynamic and thermodynamics variables are set by the 6-hourly wind (u, v, and w) and air temperature is provided by ERA-Interim on a regular 0.75° × 0.75° latitude–longitude grid. The relative humidity field is recomputed for the 500-hPa pressure level. This pressure level has been shown to be very a good proxy that encompasses the spatial and temporal variabilities of UTH (Brogniez et al. 2009). The backward integration is done over 12 days, following Roca et al. (2005), or until the air parcels encounter deep convection. Deep convection is defined with an instantaneous rain rate threshold of 5 cm h^{-1} diagnosed from ERA-Interim large-scale and convective precipitation.

A comparison between the UTH in SAPHIR and in ERA-Interim is shown in Fig. 7, with a Taylor diagram on which the four OND periods are considered

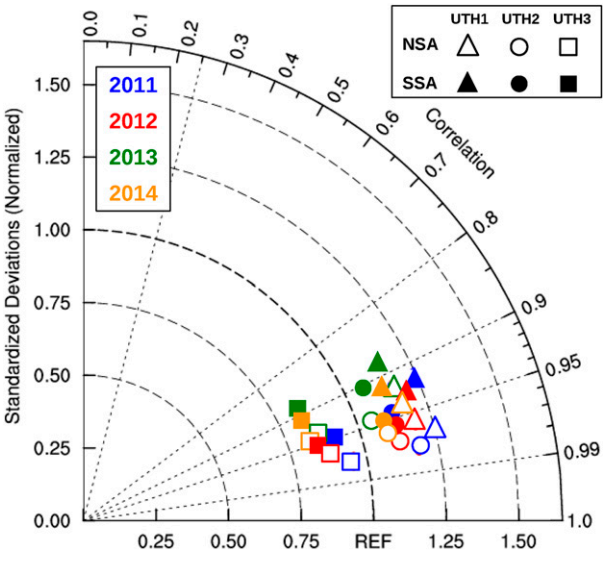

FIG. 7. Taylor diagram describing the similarities between UTHs from SAPHIR and UTHs from ERA-Interim over NSA (open symbols) and over SSA (filled symbols) during four OND seasons. Correlations are significant at 0.25 according to a 1% risk t test.

separately. The correlation ranges between 0.85 (UTH3 in OND 2013 over the SSA domain) and 0.98 (UTH3 in OND 2011 over the NSA domain). Using the CSU radiosoundings rather than the ERA-Interim dataset leads to a very similar comparison (Fig. 3). ERA-Interim underestimates the intraseasonal variability of UTH3 observed with SAPHIR (NSD < 1), while it produces slightly too-strong variations in UTH2 and even stronger variations in UTH1 (NSD = 1.14). There is a better agreement between the UTH in SAPHIR and in ERA-Interim during OND 2011, and the agreement is stronger over NSA ($R = 0.98$) than over SSA ($R = 0.95$). This can be explained by the assimilation of the CINDY/DYNAMO/AMIE radiosoundings into the ECMWF system. This comparison in the UTH space shows that despite differences, both capture the influence of MJO on UTH variability. Fields of the latter can thus be used to characterize the mechanisms at play.

The back-trajectory model is used to identify the origin of dry and moist air parcels using last-saturation coordinates. It is important to recall here that these coordinates are obtained for a given pressure level (500 hPa), while the UTHs encompass the variability of moisture in a rather broad range of atmospheric layers, including the 500-hPa level. The coordinates of final dehydration provide a general contribution of the large-scale dynamics but will not explain the entire variability of the UTHs observed in the NSA and SSA domains.

Because the back trajectories' initial points are four dimensional (time, longitude, latitude, and pressure), the following figures present the same results as 2D histograms (on a log scale) over two of the four dimensions, respectively. The samples used consist of all the reconstructed coordinates of last saturations of the air masses impacting NSA during the period OND 2011. First, Fig. 8 is a pressure–time diagram where the shaded gray areas are the MJO's active and suppressed phases. Composites of the distributions of the active and suppressed phases identified for this period are also represented on the right-hand side. Following the same principle, Fig. 9 is a latitude–time diagram. These two diagrams provide an insight on the role of large-scale advection involved during the transport of air masses. According to the MJO index of the Australian Bureau of Meteorology, the convectively active phases of MJO 2011 occurred during the periods 21 October–2 November, 19 November–28 November, and 13 December–23 December, as documented by Johnson and Ciesielski (2013) and Tseng et al. (2015). The other days are overall considered as belonging to suppressed phases, with no or little

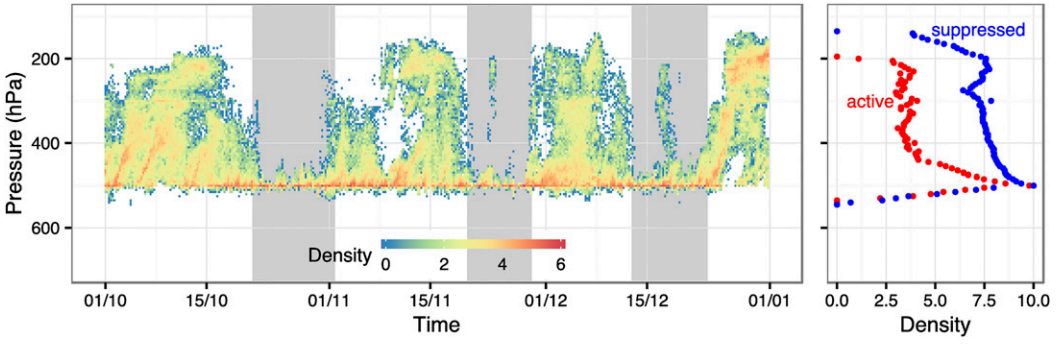

FIG. 8. (left) Pressure–time diagram of the zonal and meridional integrated distributions (with a natural log scale) of the airmass last-saturation positions. The period OND 2011 is considered for air masses landing in the NSA area (0°–8°N; 73°–80°E). The MJO-related active periods of convection are shaded in gray. (right) The cumulated distributions in pressure coordinates over active (red) and suppressed (blue) phases.

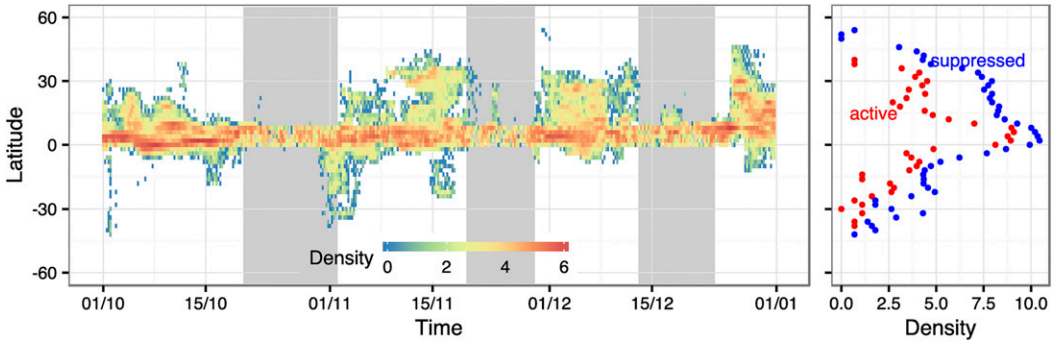

FIG. 9. As in Fig. 8, but for a latitude–time diagram of the zonal and vertical integration of the airmass last-saturation positions.

convective activity. Bursts of distant dehydration positions alternate with periods of locally restricted transport. During the suppressed phases, the large-scale flows drive air parcels from the upper troposphere (up to 200–150 hPa in Fig. 8) and from the edges of the tropical belt (until 30°–40°N–S in Fig. 9) to the NSA domain. On the contrary, during the active phases, back trajectories are interrupted much earlier by heavy rainfall, which restricts the final dehydration position to be very close to the NSA domain. The patterns are similar for the other three years (not shown).

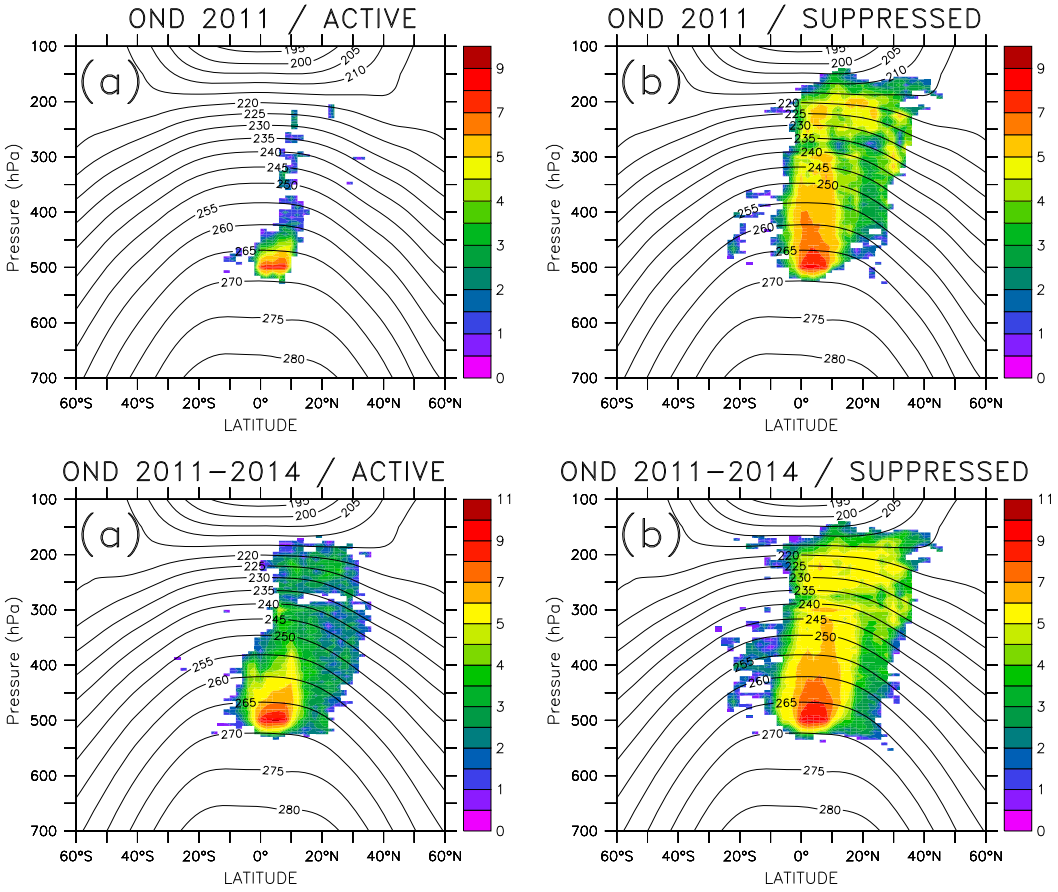

FIG. 10. Temporal integration of the airmass last-saturation positions composited over the OND months of (top) 2011 and (bottom) 2011–2014. The (a) active and (b) suppressed periods are considered separately. Contours are for the mean air temperature from the ERA-Interim averaged over the globe for the same periods.

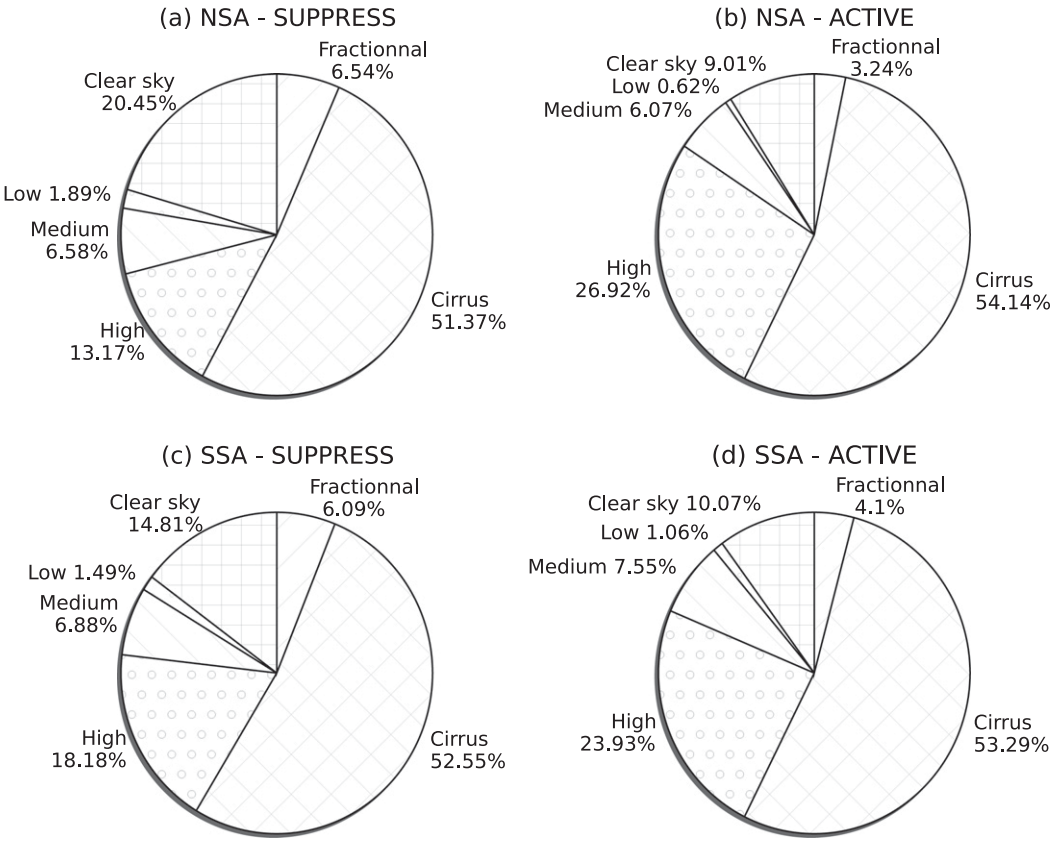

FIG. 11. Frequency of occurrence of the six cloud types over (a),(b) NSA and (c),(d) SSA computed over OND 2011 to 2014 for (left) suppressed phases and (right) active phases.

Following again the same principle as Figs. 8 and 9, Figs. 10a and 10b present the densities of the last-saturation coordinates in pressure–latitude diagrams for the active (Fig. 10a) and suppressed (Fig. 10b) periods of OND 2011–14 for the NSA domain. The mean air temperature is also represented; there is a distinct upper-tropospheric pocket of temperatures around 220–230 K (near 250–300 hPa) that brings cold and thus dry air parcels into the NSA domain during the suppressed periods. The diagrams obtained for SSA are not shown but reveal similar patterns that are roughly symmetric around the equator.

b. Assessment of the cloudiness over NSA and SSA

The UTH variability is analyzed in parallel to the cloud type occurrence over the two sounding arrays. The frequencies of occurrence of the six cloud types defined in section 2d are shown in Fig. 11 for both the suppressed phases (Figs. 11a,c) and the active phases (Figs. 11b,d) over the NSA and SSA domains and defined over the entire period. Cirrus clouds represent more than half of the total cloud cover above both areas, regardless of the convective activity. During the active phases, high and optically thick clouds occur more frequently than they do during the suppressed phases. This is one of the main features of MJO, as stated by Zhang (2005), Lau and Wu (2010), and Riley et al. (2011). The clear-sky fraction is, as expected, more important during the suppressed phases, with a higher occurrence in the NSA (20.45% of the time) than in the SSA region (14.81% of the time). This is consistent with the description made by Johnson and Ciesielski (2013) for the 2011 MJO, which has distinct features over NSA and SSA; in 2011, there is a stronger moisture signal in the NSA than in the SSA. This can be explained by the persistence of the intertropical convergence zone (ITCZ) low, which is less modulated by the occurrence of MJO events. Low clouds play only a minor role, regardless of the considered MJO phase or domain.

To characterize the covariability of clouds and the distribution of UTH, correlation coefficients (R) are computed between the occurrence of each cloud class within the domain and each moments of the spatial PDF of $\mathrm{UTH}_{\mathrm{SAPHIR}}$ (1, 2, and 3). To this end, two-time series are built: the data are accumulated over October–December

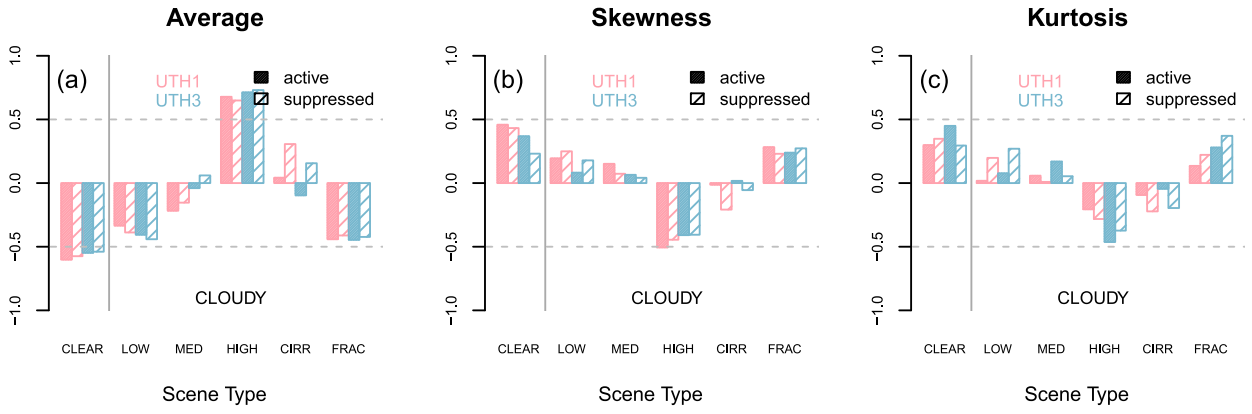

FIG. 12. Instantaneous correlation coefficients between the cloud fractions (percent) computed over the joint domain NSA–SSA and the (a) average, (b) skewness, and (c) kurtosis of the PDF of UTH1 (in red) and UTH3 (in blue). The computations are performed for all the active phases (filled bars) and suppressed phases (hatched bars) of MJO 2011–2014. Correlations are significant at 0.11 according to 1% risk t test.

2011–14 and are further divided in two in order to consider the both the active phases and the suppressed phases. The two domains are considered together because, as shown in Fig. 11, the occurrences of each of the cloud classes are similar. Each time series contains more than 2000 values if we consider the lower limit of three satellite overpasses per day at those latitudes. The computed correlations are significant when higher than 0.11 according to a 1% risk t test, even though one can reasonably admit that the moisture and clouds are not totally independent between two successive overpasses 102 min apart. Considering the pattern of the time lags between successive overpasses of *Megha-Tropiques*, a statistical independence test of two successive measurements is difficult to assess.

Figures 12 and 13 represent the correlation coefficient R computed between the spatial occurrence of six different scene types (clear sky and five cloud types) and three moments of the PDF of $\mathrm{UTH_{SAPHIR}}$ (i.e., average, skewness, and kurtosis) for two levels of UTH defined spatially over the merged NSA–SSA sounding arrays. The overlap between UTH1, UTH2, and UTH3 allows us to focus only on UTH1 and UTH3 to grasp the vertical evolution of the moisture distribution. The high-cloud fraction is significantly correlated with the evolution of UTH1–3: $R > 0.6$ with respect to the spatial average of UTH during both phases. This correlation is also seen with $R < -0.4$ with respect to the skewness and $-0.2 > R > -0.4$ with respect to the kurtosis. This means that the presence >of high-top clouds, which are mainly deep convective clouds, is associated to a PDF of UTH that becomes symmetric (the skewness diminishes) and flattens (the kurtosis also diminishes). This strong relationship between the UTH and the occurrence of high opaque clouds has already been highlighted in previous studies. Gray et al. (1975), Soden and Fu (1995), Udelhofen and Hartmann (1995), Savtchenko (2009), and Sherwood et al. (2010), among others, have

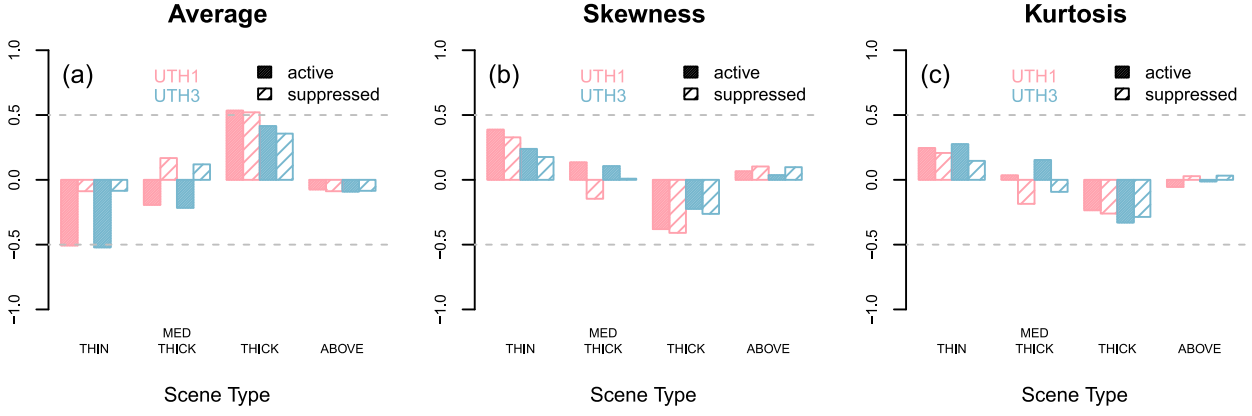

FIG. 13. As in Fig. 12, but the correlation coefficients are computed for the fraction of occurrence of the four classes of cirrus.

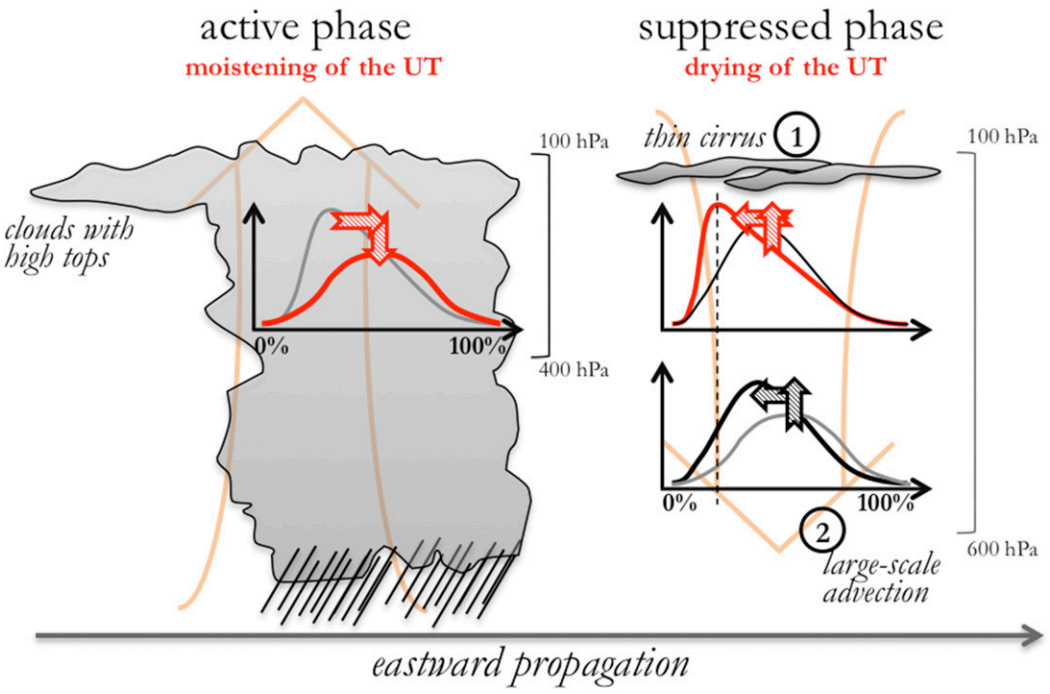

FIG. 14. Schematic that summarizes the global moistening and drying processes during the active phases of MJO and during the suppressed phases of MJO.

presented unambiguous evidence that deep convective clouds and their associated detrainment humidify the upper troposphere within tropical latitudes. Sassi et al. (2001) and Johnson and Ciesielski (2013) have also highlighted the strong humidification of the upper troposphere by the vertical transport of moisture over the Indian Ocean induced by deep convection during MJO.

Clear-sky fraction is also significantly anticorrelated with the evolution of UTH regardless of the phase of MJO: $R < -0.5$ with respect to the average, $R < -0.4$ with respect to the mode, $0.2 < R < 0.4$ with respect to the skewness, and $R > 0.2$ with respect to the kurtosis. The PDF of UTH is then positively skewed with a long tail toward the high range of humidity and a pronounced peak. The correlation with low clouds is similar, although weaker, which can be mainly explained by the fact that UTH is by definition restricted to the upper-atmospheric layers for which the low clouds are roughly considered as clear air (Brogniez et al. 2006).

The fractional clouds are generally related to a dry upper troposphere: $R < -0.4$ with respect to the average, $R < -0.3$ with respect to the mode, $R > 0.2$ with respect to the skewness, and $R > 0.15$ with respect to the kurtosis. The values of R are quite similar for the two phases except for kurtosis that reaches higher values (strongly peaked distribution) during the suppressed phases, the maxima being obtained for UTH3. This result suggests that fractional clouds are somewhat frequently associated with more peaked distribution of UTH toward the dry end of the humidity spectrum. This is consistent with the results of Radke and Hobbs (1991), Perry and Hobbs (1996), and Laird (2005) highlighting the existence of humidity halos (i.e., regions of enhanced humidity surrounding the clouds) located on the downshear, cross-shear, and upshear sides of small-to-medium-sized isolated cumulus clouds, leading to these peaked distributions of UTH at the synoptic scale.

The cirrus type embraces four types that involve different processes, which results in a strongly diluted signal: the values of R are merely significant during the active periods. For instance, Jensen et al. (1996, 2001) suggest that the formation of optically thin cirrus (cloud class "thin") near the tropical tropopause might account for the dehydration of the upper troposphere. Luo and Rossow (2004) and Soden (2004) as well as Chung et al. (2007) relate the observed covariability of UTH and cirrus anvils (cloud class "thick") to vertical motion that both maintains and creates these anvils and increases the moisture content, the evaporation of condensate being ruled out as a significant moisture source. As shown in Fig. 13, the correlation coefficients between the four types of cirrus and the moments of the PDF of UTH are consistent with these findings. The thick cirrus fraction is significantly correlated with the distribution of UTH: $0.4 < R < 0.6$ with respect to the average of UTH during both phases, $-0.4 < R < -0.2$ with respect to the

skewness and the kurtosis. This correlation profile (strongest correlations during the active phase) is very similar to that of high clouds (Fig. 13 and Fig. 14). Indeed, most of the time, thick cirrus are anvils associated with the presence of high convective clouds (Soden 2004). These anvils and their associated humidification are both the result of the deep convective activity and of the general vertical motion that brings moisture upward from the lowest layers. Similarly, the thin cirrus fraction is significantly anticorrelated with the distribution of UTH regardless of the phase of the MJO: $-0.5 < R < -0.3$ with respect to the average, $-0.5 < R < -0.2$ with respect to the mode, $0.2 < R < 0.4$ with respect to the skewness, and $R > 0.2$ with respect to the kurtosis. In such situations, these clouds are associated to a long-tailed PDF of humidity peaking in the dry end of the humidity spectrum.

5. Summary and discussion

The role of large-scale processes and cloud-related processes on the distribution of UTH when the development of MJO takes place in the Indian Ocean was analyzed using UTH data retrieved from SAPHIR onboard *Megha-Tropiques*. In addition to SAPHIR measurements, a Lagrangian transport model with ERA-Interim four-dimensional (4D) winds and temperature fields as inputs was used to examine the origin of the air masses located in the northern sounding array region and the southern sounding array region during the CINDY/DYNAMO/AMIE field campaign. The frequency of occurrence of six main cloud types defined by the SAFNWC and projected at the SAPHIR pixel level provided further information about the joint evolution of cloudiness and UTH. The distribution of UTH was characterized in terms of the statistical moments by calculating its average, mode, skewness, and kurtosis for each overpass of *Megha-Tropiques* during the four consecutive winters 2011–14. The results are summarized on the schematic of Fig. 14 and show the following:

1) There is a strong difference in the distribution of UTH according to the phase of MJO (active or suppressed). During active (suppressed) phases, the PDFs of the three layers of $\mathrm{UTH_{SAPHIR}}$ are moister (drier) and are negatively (positively) skewed. From the upper (UTH1) down to the middle (UTH3) troposphere, the skewness of the PDFs also evolves from peaked to flatter distributions, thus highlighting the importance of different distribution properties according to the convective activity and to the atmospheric layer considered.
2) The domain of origin of the air masses that finish their trajectories within NSA or SSA varies between the composites of the active and suppressed MJO phases. Computations using the back-trajectory model are spatially constrained by the enhanced convective activity occurring in the Indian Ocean Basin. But there is a clear contribution of an upper-tropospheric (200–150 hPa) westerly flow to the instantaneous variability of UTH.
3) The joint analysis with the cloud types identified in the NSA and SSA domains shows a strong relationship between UTH and cloud cover, especially for high opaque clouds and fractional clouds. Relationships between cloud fractions and distribution of UTH are overall quite similar regardless of convective activity except for the fraction of cirrus clouds. The occurrence of thin cirrus clouds is strongly associated with a dry upper troposphere (stronger relationship during the suppressed phases), and the occurrence of thick cirrus clouds is related to a moist upper troposphere.

The lateral mixing of air masses is one of the mechanisms producing dry air in the tropical and subtropical atmosphere (e.g., Pierrehumbert and Yang 1993; Galewsky et al. 2005). However, different transport processes dominate in the different sectors of the tropical belt. The intrusion of dry air of stratospheric origin via Rossby waves breaking, strongly influences the variability of UTH in a large part of the tropics (Gettelman et al. 2006). In regions influenced by the fluctuations of MJO, the subtropical UTH is related to the location and strength of the winter subtropical anticyclones (Ryoo et al. 2008).

It is important to further examine several aspects of the analysis presented here. One aspect is the asymmetry of the variability between the two domains (NSA and SSA) since the mechanisms at play in determining the distribution and the variability of UTH are obviously different between the two hemispheres. For instance, Ryoo et al. (2008) have shown that the slow eastward-propagating patterns of UTH observed in the northern subtropical Indian Ocean are not seen to the southern subtropics.

Another aspect deserving further examination is that MJO events in the same season have different dynamics, as highlighted by Johnson and Ciesielski (2013) for the 2011 MJO. The eight phases characterizing the MJO have been merged into two periods, one globally active and one globally suppressed. But the moistening and drying processes of the MJO activity are sensibly different: the convective centers have very different characteristics, with maritime and continental locations. Compositing along the eight phases would strengthen

these results and enable a detailed analysis of the role of the different processes.

Finally, it would be of great interest to fit a statistical model of a unique form of distribution law of the free tropospheric RH as derived by Sherwood et al. (2006). This model could then be used to analyze the occurrence of cloud types and the dynamical processes involved. Cloud cover and total water in the column are strongly related at the subgrid scale (Tompkins 2002; Tompkins and Janisková 2004). An important step in improving the parameterization of subgrid convection could be to go down to the cloud type (and not only to the cloud fraction), to the water vapor (and not to the total column of water), and to use a fixed diagnostic relationship for the higher-order moments of the PDF of RH.

Acknowledgments. The authors are thankful to Christophe Dufour (LATMOS) for his work on the UTH scientific algorithm and for its maintenance. The support of K. Ramage and S. Bouffiès-Cloché and the IPSL data server Climserv is also appreciated. The UTH data are available from the French ground segment hosted by the ICARE Data and Service Center. We thank Nicolas Henriot and the entire staff of ICARE for supporting the products and for processing the UTH. The CNES is acknowledged for its financial support of the scientific activities during the *Megha-Tropiques* mission; R. Fallourd's research is directly supported by CNES. The array-averaged CINDY/DYNAMO/AMIE meteorological parameters used in this study are available from the National Center for Atmospheric Research (NCAR) Earth Observation Laboratory (EOL) DYNAMO archive, and P. Ciesielski and R. Johnson of CSU are thanked for making it available. Finally, the three anonymous reviewers are acknowledged for their constructive comments that improved the manuscript.

APPENDIX

Moments of a Distribution Function *f*(*X*)

The probability distribution function f of real variable X is characterized by its four moments.

1) The first moment is the average, which is the arithmetic mean of all n values:

$$E(X) = \frac{1}{n}\sum_{i=1}^{n} X_i.$$

2) The second moment is the mode, which is the output value that is most likely to occur for a continuous distribution. The mode is determined by the point at which the gradient of the cumulative distribution is at its maximum. If the distribution follows a normal law, then average and mode have the same value.

3) The third moment is the skewness S that gives an indication on the asymmetry of the distribution $f(X)$ according to its variance σ_X:

$$S = \frac{1}{n}\sum_{i=1}^{n}\left[\frac{X_i - E(X_i)}{\sigma_X}\right]^3.$$

If $0 < S < 1$, then the distribution is negatively skewed, meaning that the tail is longer on the left-hand side of the mode. If $S = 1$, the distribution is symmetric. If $S > 1$, the distribution is positively skewed, meaning that the tail is longer on the right-hand side of the mode.

4) The fourth moment is the kurtosis K that indicates the peakedness of the distribution $f(X)$:

$$K = \frac{1}{n}\sum_{i=1}^{n}\left[\frac{\mathrm{UTH}_i - E(\mathrm{UTH})}{\sigma_{\mathrm{UTH}}}\right]^4 - 3 \quad \text{and}$$

$$K = \frac{1}{n}\sum_{i=1}^{n}\left[\frac{X_i - E(X_i)}{\sigma_X}\right]^4 - 3.$$

If $K > 3$, then the distribution is named leptokurtic and has heavy tails. If $K < 3$, then the distribution is named platykurtic and has light tails. If $K = 3$, then the distribution is named mesokurtic.

REFERENCES

Allan, R. P., M. A. Ringer, and A. Slingo, 2003: Evaluation of moisture in the Hadley Centre climate model using simulations of HIRS water-vapour channel radiances. *Quart. J. Roy. Meteor. Soc.*, **129**, 3371–3389, doi:10.1256/qj.02.217.

Brogniez, H., and R. T. Pierrehumbert, 2006: Using microwave observations to assess large-scale control of the free tropospheric water vapor in the mid-latitudes. *Geophys. Res. Lett.*, **33**, L14801, doi:10.1029/2006GL026240.

——, R. Roca, and L. Picon, 2006: A clear-sky radiance archive from Meteosat "water vapor" observations. *J. Geophys. Res.*, **111**, D21109, doi:10.1029/2006JD007238.

——, ——, and ——, 2009: A study of the free tropospheric humidity interannual variability using Meteosat data and an advection–condensation transport model. *J. Climate*, **22**, 6773–6787, doi:10.1175/2009JCLI2963.1.

——, P. E. Kirstetter, and L. Eymard, 2013: Expected improvements in the atmospheric humidity profile retrieval using the Megha-Tropiques microwave payload. *Quart. J. Roy. Meteor. Soc.*, **139**, 842–851, doi:10.1002/qj.1869.

——, G. Clain, and R. Roca, 2015: Validation of upper-tropospheric humidity from SAPHIR onboard *Megha-Tropiques* using tropical soundings. *J. Appl. Meteor. Climatol.*, **54**, 896–908, doi:10.1175/JAMC-D-14-0096.1.

Camargo, S. J., M. C. Wheeler, and A. H. Sobel, 2009: Diagnosis of the MJO modulation of tropical cyclogenesis using an empirical index. *J. Atmos. Sci.*, **66**, 3061–3074, doi:10.1175/2009JAS3101.1.

Chung, E. S., B. J. Sohn, J. Schmetz, and M. Koenig, 2007: Diurnal variation of upper tropospheric humidity and its relations to convective activities over tropical Africa. *Atmos. Chem. Phys.*, **7**, 2489–2503, doi:10.5194/acp-7-2489-2007.

Colman, R., 2003: A comparison of climate feedbacks in general circulation models. *Climate Dyn.*, **20**, 865–873.

Dee, D. P., and S. Uppala, 2009: Variational bias correction of satellite radiance data in the ERA-Interim reanalysis. *Quart. J. Roy. Meteor. Soc.*, **135**, 1830–1841, doi:10.1002/qj.493.

——, and Coauthors, 2011: The ERA-Interim reanalysis: Configuration and performance of the data assimilation system. *Quart. J. Roy. Meteor. Soc.*, **137**, 553–597, doi:10.1002/qj.828.

Derrien, M., and H. Le Gléau, 2003: SAFNWC/MSG SEVIRI cloud products. *Proc. 2002 EUMETSAT Meteorological Satellite Conf.*, Weimar, Germany, European Organisation for the Exploitation of Meteorological Satellites, 191–198.

——, and ——, 2010: Improvement of cloud detection near sunrise and sunset by temporal-differencing and region-growing techniques with real-time SEVIRI. *Int. J. Remote Sens.*, **31**, 1765–1780, doi:10.1080/01431160902926632.

Desbois, M., M. Capderou, L. Eymard, R. Roca, N. Viltard, M. Viollier, and N. Karouche, 2007: *Megha-Tropiques*: Un satellite hydrométéorologique franco-indien. *Météorologie*, **57**, 19–27, doi:10.4267/2042/18185.

Dessler, A. E., and K. Minschwaner, 2007: An analysis of the regulation of tropical tropospheric water vapor. *J. Geophys. Res.*, **112**, D10120, doi:10.1029/2006JD007683.

——, and S. C. Sherwood, 2009: A matter of humidity. *Science*, **323**, 1020–1021, doi:10.1126/science.1171264.

Eyre, J., 1991: A fast radiative transfer model for satellite sounding systems. ECMWF Tech. Memo. 176, 28 pp. [Available online at https://www.ecmwf.int/en/elibrary/9329-fast-radiative-transfer-model-satellite-sounding-systems.]

Galewsky, J., A. Sobel, and I. Held, 2005: Diagnosis of subtropical humidity dynamics using tracers of last saturation. *J. Atmos. Sci.*, **62**, 3353–3367, doi:10.1175/JAS3533.1.

Gettelman, A., W. D. Collins, E. J. Fetzer, A. Eldering, F. W. Irion, P. B. Duffy, and G. Bala, 2006: Climatology of upper-tropospheric relative humidity from the Atmospheric Infrared Sounder and implications for climate. *J. Climate*, **19**, 6104–6121, doi:10.1175/JCLI3956.1.

Gray, W. M., E. Ruprecht, and R. Phelps, 1975: Relative humidity in tropical weather systems. *Mon. Wea. Rev.*, **103**, 685–690, doi:10.1175/1520-0493(1975)103<0685:RHITWS>2.0.CO;2.

IPCC, 2013: *Climate Change 2013: The Physical Science Basis.* Cambridge University Press, 1535 pp., doi:10.1017/CBO9781107415324.

Jensen, E. J., O. B. Toon, L. Pfister, and H. B. Selkirk, 1996: Dehydration of the upper troposphere and lower stratosphere by subvisible cirrus clouds near the tropical tropopause. *Geophys. Res. Lett.*, **23**, 825–828, doi:10.1029/96GL00722.

——, L. Pfister, A. S. Ackerman, A. Tabazadeh, and O. B. Toon, 2001: A conceptual model of the dehydration of air due to freeze-drying by optically thin, laminar cirrus rising slowly across the tropical tropopause. *J. Geophys. Res.*, **106**, 17 237–17 252, doi:10.1029/2000JD900649.

Johnson, R. H., and P. E. Ciesielski, 2013: Structure and properties of Madden–Julian oscillations deduced from DYNAMO sounding arrays. *J. Atmos. Sci.*, **70**, 3157–3179, doi:10.1175/JAS-D-13-065.1.

Laird, N. F., 2005: Humidity halos surrounding small cumulus clouds in a tropical environment. *J. Atmos. Sci.*, **62**, 3420–3425, doi:10.1175/JAS3538.1.

Lau, K. M., and H. T. Wu, 2010: Characteristics of precipitation, cloud, and latent heating associated with the Madden–Julian oscillation. *J. Climate*, **23**, 504–518, doi:10.1175/2009JCLI2920.1.

Liu, Y. S., S. Fueglistaler, and P. H. Haynes, 2010: Advection-condensation paradigm for stratospheric water vapor. *J. Geophys. Res.*, **115**, D24307, doi:10.1029/2010JD014352.

Luo, Z., and W. B. Rossow, 2004: Characterizing tropical cirrus life cycle, evolution, and interaction with upper-tropospheric water vapor using Lagrangian trajectory analysis of satellite observations. *J. Climate*, **17**, 4541–4563, doi:10.1175/3222.1.

Madden, R. A., and P. R. Julian, 1971: Detection of a 40–50 day oscillation in the zonal wind in the tropical Pacific. *J. Atmos. Sci.*, **28**, 702–708, doi:10.1175/1520-0469(1971)028<0702:DOADOI>2.0.CO;2.

——, and ——, 1972: Description of global-scale circulation cells in the tropics with a 40–50 day period. *J. Atmos. Sci.*, **29**, 1109–1123, doi:10.1175/1520-0469(1972)029<1109:DOGSCC>2.0.CO;2.

Matricardi, M., F. Chevallier, G. Kelly, and J.-N. Thépaut, 2004: An improved general fast radiative transfer model for the assimilation of radiance observations. *Quart. J. Roy. Meteor. Soc.*, **130**, 153–173, doi:10.1256/qj.02.181.

Morcrette, J. J., 1991: Evaluation of model-generated cloudiness: Satellite-observed and model-generated diurnal variability of brightness temperature. *Mon. Wea. Rev.*, **119**, 1205–1224, doi:10.1175/1520-0493(1991)119<1205:EOMGCS>2.0.CO;2.

Pai, D. S., J. Bhate, O. P. Sreejith, and H. R. Hatwar, 2011: Impact of MJO on the intraseasonal variation of summer monsoon rainfall over India. *Climate Dyn.*, **36**, 41–55, doi:10.1007/s00382-009-0634-4.

Perry, K. D., and P. V. Hobbs, 1996: Influences of isolated cumulus clouds on the humidity of their surroundings. *J. Atmos. Sci.*, **53**, 159–174, doi:10.1175/1520-0469(1996)053<0159:IOICCO>2.0.CO;2.

Picon, L., and M. Desbois, 1990: Relation between Meteosat water vapor radiance fields and large scale tropical circulation features. *J. Climate*, **3**, 865–876, doi:10.1175/1520-0442(1990)003<0865:RBMWVR>2.0.CO;2.

Pierrehumbert, R. T., and H. Yang, 1993: Global chaotic mixing on isentropic surfaces. *J. Atmos. Sci.*, **50**, 2462–2480, doi:10.1175/1520-0469(1993)050<2462:GCMOIS>2.0.CO;2.

——, and R. Roca, 1998: Evidence for control of Atlantic subtropical humidity by large scale advection. *Geophys. Res. Lett.*, **25**, 4537–4540, doi:10.1029/1998GL900203.

——, H. Brogniez, and R. Roca, 2007: On the relative humidity of the Earth's atmosphere. *The Global Circulation of the Atmosphere*, T. Schneider and A. H. Sobel, Eds., Princeton University Press, 143–185.

Radke, L. F., and P. V. Hobbs, 1991: Humidity and particle fields around some small cumulus clouds. *J. Atmos. Sci.*, **48**, 1190–1193, doi:10.1175/1520-0469(1991)048<1190:HAPFAS>2.0.CO;2.

Riley, E. M., B. E. Mapes, and S. N. Tulich, 2011: Clouds associated with the Madden–Julian oscillation: A new perspective from *CloudSat*. *J. Atmos. Sci.*, **68**, 3032–3051, doi:10.1175/JAS-D-11-030.1.

Roca, R., M. Viollier, L. Picon, and M. Desbois, 2002: A multisatellite analysis of deep convection and its moist environment

over the Indian Ocean during the winter monsoon. *J. Geophys. Res.*, **107**, 8012, doi:10.1029/2000JD000040.

——, J.-P. Lafore, C. Piriou, and J.-L. Redelsperger, 2005: Extratropical dry-air intrusions into the West African monsoon midtroposphere: An important factor for the convective activity over the Sahel. *J. Atmos. Sci.*, **62**, 390–407, doi:10.1175/JAS-3366.1.

——, and Coauthors, 2015: The *Megha-Tropiques* mission: A review after three years in orbit. *Front. Earth Sci.*, **3**, 0017, doi:10.3389/feart.2015.00017.

Rossow, W. B., and R. A. Schiffer, 1991: ISCCP cloud data products. *Bull. Amer. Meteor. Soc.*, **72**, 2–20, doi:10.1175/1520-0477(1991)072<0002:ICDP>2.0.CO;2.

Ryoo, J.-M., D. Waugh, and A. Gettelman, 2008: Variability of subtropical upper tropospheric humidity. *Atmos. Chem. Phys.*, **8**, 2643–2655, doi:10.5194/acp-8-2643-2008.

Sassi, F., M. Salby, and W. G. Read, 2001: Relationship between upper-tropospheric humidity and deep convection. *J. Geophys. Res.*, **106**, 17 133–17 146, doi:10.1029/2001JD900121.

Saunders, R., and Coauthors, 2013: RTTOV-11 science and validation report. EUMETSAT Rep. NWPSAF-MO-TV-032, 62 pp. [Available online at http://nwpsaf.eu/oldsite/deliverables/rtm/docs_rttov11/rttov11_svr.pdf.]

Savtchenko, A., 2009: Deep convection and upper-tropospheric humidity: A look from the A-Train. *Geophys. Res. Lett.*, **36**, L06814, doi:10.1029/2009GL037508.

Schmetz, J., C. Geijo, W. Menzel, K. Strabala, L. Van De Berg, K. Holmlund, and S. Tjemkes, 1995: Satellite observations of upper tropospheric relative humidity, clouds and wind field divergence. *Contrib. Atmos. Phys.*, **68**, 345–357.

Sèze, G., J. Pelon, M. Derrien, H. L. Gléau, and B. Six, 2015: Evaluation against *CALIPSO* lidar observations of the multi-geostationary cloud cover and type dataset assembled in the framework of the Megha-Tropiques mission. *Quart. J. Roy. Meteor. Soc.*, **141**, 774–797, doi:10.1002/qj.2392.

Sherwood, S. C., E. Kursinsky, and W. Read, 2006: A distribution law for free-tropospheric relative humidity. *J. Climate*, **19**, 6267–6277, doi:10.1175/JCLI3978.1.

——, R. Roca, T. M. Weckwerth, and N. G. Andronova, 2010: Tropospheric water vapor, convection, and climate. *Rev. Geophys.*, **48**, RG2001, doi:10.1029/2009RG000301.

Soden, B. J., 2004: The impact of tropical convection and cirrus on upper tropospheric humidity: A Lagrangian analysis of satellite measurements. *Geophys. Res. Lett.*, **31**, L20104, doi:10.1029/2004GL020980.

——, and F. P. Bretherton, 1993: Upper tropospheric relative humidity from the GOES 6.7 μm channel: Method and climatology for July 1987. *J. Geophys. Res.*, **98**, 16 669–16 688, doi:10.1029/93JD01283.

——, and R. Fu, 1995: A satellite analysis of deep convection, upper-tropospheric humidity, and the greenhouse effect. *J. Climate*, **8**, 2333–2351, doi:10.1175/1520-0442(1995)008<2333:ASAODC>2.0.CO;2.

——, and I. M. Held, 2006: An assessment of climate feedbacks in coupled ocean–atmosphere models. *J. Climate*, **19**, 3354–3360, doi:10.1175/JCLI3799.1.

Su, H., W. G. Read, J. H. Jiang, J. W. Waters, D. L. Wu, and E. J. Fetzer, 2006: Enhanced positive water vapor feedback associated with tropical deep convection: New evidence from Aura MLS. *Geophys. Res. Lett.*, **33**, L05709, doi:10.1029/2005GL025505.

Taylor, K. E., 2001: Summarizing multiple aspects of model performance in a single diagram. *J. Geophys. Res.*, **106**, 7183–7192, doi:10.1029/2000JD900719.

Tompkins, A. M., 2002: A prognostic parameterization for the subgrid-scale variability of water vapor and clouds in large-scale models and its use to diagnose cloud cover. *J. Atmos. Sci.*, **59**, 1917–1942, doi:10.1175/1520-0469(2002)059<1917:APPFTS>2.0.CO;2.

——, and M. Janisková, 2004: A cloud scheme for data assimilation: Description and initial tests. *Quart. J. Roy. Meteor. Soc.*, **130**, 2495–2517, doi:10.1256/qj.03.162.

Tseng, K. C., C. H. Sui, and T. Li, 2015: Moistening processes for Madden–Julian oscillations during DYNAMO/CINDY. *J. Climate*, **28**, 3041–3057, doi:10.1175/JCLI-D-14-00416.1.

Udelhofen, P. M., and D. L. Hartmann, 1995: Influence of tropical cloud systems on the relative humidity in the upper troposphere. *J. Geophys. Res.*, **100**, 7423–7440, doi:10.1029/94JD02826.

Wheeler, M. C., and H. H. Hendon, 2004: An all-season real-time multivariate MJO index: Development of an index for monitoring and prediction. *Mon. Wea. Rev.*, **132**, 1917–1932, doi:10.1175/1520-0493(2004)132<1917:AARMMI>2.0.CO;2.

——, ——, S. Cleland, H. Meinke, and A. Donald, 2009: Impacts of the MJO on Australian rainfall and circulation. *J. Climate*, **22**, 1482–1497, doi:10.1175/2008JCLI2595.1.

Zelinka, M. D., and D. L. Hartmann, 2009: Response of humidity and clouds to tropical deep convection. *J. Climate*, **22**, 2389–2404, doi:10.1175/2008JCLI2452.1.

Zhang, C., 2005: Madden-Julian oscillation, *Rev. Geophys.*, **43**, RG2003, doi:10.1029/2004RG000158.

——, 2013: Madden–Julian oscillation: Bridging weather and climate. *Bull. Amer. Meteor. Soc.*, **94**, 1849–1870, doi:10.1175/BAMS-D-12-00026.1.

——, B. Mapes, and B. Soden, 2003: Bimodality in tropical water vapour. *Quart. J. Roy. Meteor. Soc.*, **129**, 2847–2866, doi:10.1256/qj.02.166.